Image-Processing Technique for Suppressing Ribs in Chest Radiographs by Means of Massive Training Artificial Neural Network (MTANN)

Kenji Suzuki*, *Senior Member, IEEE*, Hiroyuki Abe, Heber MacMahon, and Kunio Doi

***Abstract*—When lung nodules overlap with ribs or clavicles in chest radiographs, it can be difficult for radiologists as well as computer-aided diagnostic (CAD) schemes to detect these nodules. In this paper, we developed an image-processing technique for suppressing the contrast of ribs and clavicles in chest radiographs by means of a multiresolution massive training artificial neural network (MTANN). An MTANN is a highly nonlinear filter that can be trained by use of input chest radiographs and the corresponding "teaching" images. We employed "bone" images obtained by use of a dual-energy subtraction technique as the teaching images. For effective suppression of ribs having various spatial frequencies, we developed a multiresolution MTANN consisting of multiresolution decomposition/composition techniques and three MTANNs for three different-resolution images. After training with input chest radiographs and the corresponding dual-energy bone images, the multiresolution MTANN was able to provide "bone-image-like" images which were similar to the teaching bone images. By subtracting the bone-image-like images from the corresponding chest radiographs, we were able to produce "soft-tissue-image-like" images where ribs and clavicles were substantially suppressed. We used a validation test database consisting of 118 chest radiographs with pulmonary nodules and an independent test database consisting of 136 digitized screen-film chest radiographs with 136 solitary pulmonary nodules collected from 14 medical institutions in this study. When our technique was applied to nontraining chest radiographs, ribs and clavicles in the chest radiographs were suppressed substantially, while the visibility of nodules and lung vessels was maintained. Thus, our image-processing technique for rib suppression by means of a multiresolution MTANN would be potentially useful for radiologists as well as for CAD schemes in detection of lung nodules on chest radiographs.**

***Index Terms*—Artificial neural network, chest radiography, computer-aided diagnosis (CAD), dual-energy subtraction, lung nodule, rib suppression.**

I. Introduction

CHEST radiography is the most frequently used diagnostic imaging examination for chest diseases such as lung cancer, tuberculosis, pneumonia, pneumoconioses, and pulmonary emphysema. More than 9 million people worldwide die annually from chest diseases [1]. Lung cancer causes 945 000 deaths [1], and is the leading cause of cancer deaths in the world [1] and in countries [2] such as the United States, the United Kingdom, the Russian Federation, Canada, Poland, and Japan. In the United States alone, lung cancer is expected to cause 160 440 deaths in 2004 [3]. Chest radiographs have been used for detection of lung cancer [4]–[6] because some evidence suggests that early detection of lung cancer may allow a favorable prognosis [7]–[9]. Lung nodules (i.e., potential lung cancers) in chest radiographs, however, can be overlooked by radiologists in from 12%–90% of cases in which nodules are visible in retrospect [10], [11]. Many, 82%–95%, of the missed lung cancers were partly obscured by overlying bones such as ribs and/or a clavicle [10], [11]. Therefore, a computer-aided diagnostic (CAD) scheme [12], [13] for nodule detection on chest radiographs has been investigated, because the computer prompts indicating nodules could improve radiologists' detection accuracy [14]–[16].

A major challenge in current CAD schemes [17]–[27] for nodule detection on chest radiographs is the detection of nodules overlapping with ribs, rib crossings, and clavicles, because a majority of false positives are caused by these structures [18], [28]. This results in lowering the sensitivity as well as the specificity of a CAD scheme. Because nodules overlapping with ribs and clavicles were reported to be difficult for radiologists to observe [29], [30], detection of such nodules is important for CAD schemes. Therefore, the suppression of ribs and clavicles in chest radiographs would be potentially useful for improving radiologists' detection accuracy as well as the CAD performance.

Our purpose in this study was to develop an image-processing technique for suppressing the contrast of ribs in chest radiographs by means of a multiresolution massive training artificial neural network (MTANN).

II. Materials and Methods

A. Massive Training Artificial Neural Network (MTANN)

In the field of image processing, supervised nonlinear image-processing techniques [31]–[34] based on an artificial neural network (ANN), called a "neural filter" [32] and a "neural edge enhancer" [33], [34], have been investigated for reduction of the quantum mottle (specific noise observed in medical x-ray images) in angiograms and radiographs [35] and for supervised detection of left ventricular contours traced by cardiologists in angiography [36], respectively. By extending the neural filter and the neural edge enhancer, MTANNs [37] have been developed to accommodate the task of distinguishing a specific opacity from other opacities in medical images. MTANNs have been applied for reduction of false positives in

Manuscript received October 21, 2005; revised January 16, 2006. This work was supported in part by the United States Public Health Service (USPHS) under Grant CA62625. *Asterisk indicates corresponding author.*

*K. Suzuki is with the Kurt Rossmann Laboratories for Radiologic Image Research, Department of Radiology, The University of Chicago, 5841 S. Maryland Ave., Chicago, IL 60637 USA (e-mail: suzuki@uchicago.edu).

H. Abe, H. MacMahon, and K. Doi are with the Department of Radiology, The University of Chicago, Chicago, IL 60637 USA.

Digital Object Identifier 10.1109/TMI.2006.871549

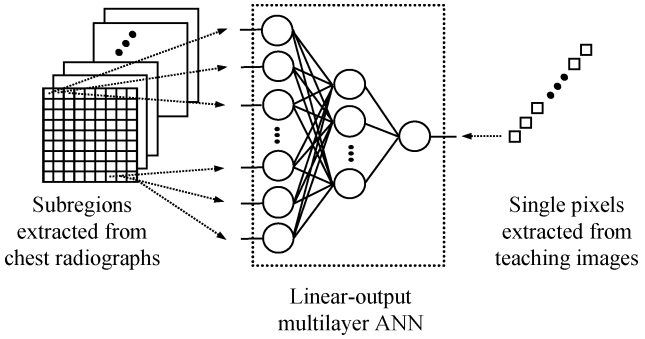

Fig. 1. Architecture and training of an MTANN consisting of a linear-output multilayer ANN model and a massive-subregions training scheme. The pixel values in the subregion extracted from a chest radiograph are entered as input to the ANN. Single pixels extracted from teaching images are used as teaching values for the corresponding subregions.

computerized detection of lung nodules in low-dose computed tomography (CT) [37], [38] and chest radiography [39], for distinction between benign and malignant lung nodules in CT [40]. In our previous studies [37]–[40], the MTANNs aimed at classification of regions-of-interest into abnormal or normal; thus, these studies were in the field of pattern recognition, whereas this paper aims at suppression of ribs in chest radiographs, which would be in the field of image processing.

The architecture and the training method of an MTANN are shown in Fig. 1. The MTANN can be considered to be a highly nonlinear filter that can be trained with input images and the corresponding "teaching" images. The MTANN consists of a linear-output multilayer ANN model [41], which is capable of operating on image data directly. The linear-output multilayer ANN model employs a linear function instead of a sigmoid function as the activation function of the unit in the output layer because the characteristics of an ANN were improved significantly with a linear function when applied to the continuous mapping of values in image processing [34], [41]. A conventional ANN hardly outputs values near zero and one because of the characteristics of a sigmoid function, whereas the linear-output multilayer ANN outputs values linearly. The training for teaching values near zero and one converges more slowly than do other values with the conventional ANN theoretically, whereas these values are trained evenly with the linear-output multilayer ANN model. This affects the convergence characteristics and the output characteristics of ANN models. Therefore, the linear-output multilayer ANN would be suitable for image processing, where the teaching values may be continuous values ranging from zero to one, whereas the conventional ANN is suitable for a classification task where the teaching values are assigned to classes (see [34], [41] for theoretical considerations). The pixel values of original chest radiographs are normalized first such that a pixel value of zero is zero and a pixel value of the maximum gray-scale level (1,023) is one. The inputs of the linear-output multilayer ANN are the pixel values in a subregion R_S extracted from a chest radiograph. The output is a continuous value, which corresponds to the center pixel in the subregion, represented by

$$f(x,y) = NN(\vec{I}_{x,y}) \tag{1}$$

where

$$\vec{I}_{x,y} = \{g(x-i, y-j) | i,j \in R_S\} \tag{2}$$

is the input vector to the MTANN, $f(x,y)$ is an estimate for a teaching value, x and y are the coordinates of the image, $NN\{\bullet\}$ is the output of the linear-output multilayer ANN, and $g(x,y)$ is a normalized pixel value in an input chest radiograph. Note that only one unit is employed in the output layer. The input vector can be rewritten as

$$\vec{I}_{x,y} = \{I_1, I_2, \cdots, I_m, \cdots, I_{N_I}\} \tag{3}$$

where m is an input unit number, and N_I is the number of input units. Because the activation functions of the units in the input layer are an identity function, the output of the nth unit in the input layer can be represented by I_n. The output of the nth unit in the hidden layer is represented by

$$O_n^H = f_S\left\{\sum_{m=1}^{N_I} w_{mn}^H \cdot I_m - w_{0n}^H\right\} \tag{4}$$

where W_{mn}^H is a weight between the mth unit in the input layer and the nth unit in the hidden layer, W_{0n}^H is an offset of the nth unit in the hidden layer, and $f_S(u)$ is a sigmoid function

$$f_S(u) = \frac{1}{1+\exp(-u)}. \tag{5}$$

The output of the unit in the output layer is represented by

$$f(x,y) = f_L\left\{\sum_{m=1}^{N_H} w_m^O \cdot O_m^H - w_0^O\right\} \tag{6}$$

where W_m^O is a weight between the mth unit in the hidden layer and the unit in the output layer, W_0^O is an offset of the unit in the output layer, $f_L(u)$ is a linear function

$$f_L(u) = a \cdot u + 0.5 \tag{7}$$

and a is a slope parameter. The entire output image is obtained by scanning of an input chest image with the MTANN.

The MTANN involves training with massive subregion-pixel pairs, where we call it a massive-subregions training scheme. Input chest radiographs are divided pixel by pixel into a large number of overlapping subregions. Single pixels corresponding to the input subregions are extracted from the teaching images as teaching values. The MTANN is massively trained by using each of a large number of the input subregions together with each of the corresponding teaching single pixels. The training set of pairs of a subregion and a teaching pixel is represented by

$$\left\{\vec{I}(x,y), T(x,y) | x,y \in R_T\right\} = \left\{(\vec{I}_1, T_1), (\vec{I}_2, T_2), \cdots, (\vec{I}_p, T_p), \cdots, \left(\vec{I}_{N_T}, T_{N_T}\right)\right\} \tag{8}$$

where $T(x,y)$ is a teaching image, R_T is a training region which corresponds to the collection of the centers of subregions (or teaching pixels), p is a pixel number in R_T, and N_T is the

number of pixels in R_T. The error to be minimized by training is defined by

$$E = \frac{1}{N_T} \sum_{x,y \in R_T} \{T(x,y) - f(x,y)\}^2 . \tag{9}$$

The MTANN is trained by a linear-output back-propagation (BP) algorithm [34], [41] which was derived for the linear-output multilayer ANN model in the same way as the BP algorithm [42], [43]. The correction of the weight between hidden units and output unit can be represented by

$$\Delta W^O = -\eta \frac{\partial E}{\partial W^O} = -\eta a (T - f) O^H \tag{10}$$

where η is a learning rate. Please refer to [34], [41] for the details and the property of the linear-output BP algorithm. After training, the MTANN is expected to produce images similar to the teaching images.

We used a dual-energy subtraction technique [44] to obtain the teaching images for MTANNs for suppression of ribs in chest radiographs. The dual-energy subtraction is a technique for separating bones from soft tissues in chest radiographs by use of the energy dependence of the x-ray attenuation by different materials; it can produce two tissue-selective images, i.e., a "bone" image and a "soft-tissue" image. Chest radiographs are used as input images to MTANNs, and the corresponding dual-energy bone images are used as the teaching images. We did not directly use dual-energy soft-tissue images as the teaching images, because the MTANNs trained with dual-energy soft-tissue images produced results that were slightly inferior to the MTANNs trained with dual-energy bone images (see details in Section IV).

B. Multiesolution Decomposition and Composition

Ribs in chest radiographs include various spatial-frequency components. For a single MTANN, suppression of ribs containing such various frequencies is difficult, because the capability of a single MTANN is limited, i.e., the capability depends on the size of the subregion of the MTANN. Because the training of the MTANN takes a substantially long time, it is difficult in practice to train the MTANN with a large subregion. In order to overcome this issue, we employed multiresolution decomposition/composition techniques [45], [46]. The multiresolution decomposition, illustrated in Fig. 2(a), is a technique for decomposing an original high-resolution image into different-resolution images. First, one obtains a medium-resolution image $g_M(x,y)$ from an original high-resolution image $g_H(x,y)$ by performing down-sampling with averaging, i.e., four pixels in the original image are replaced by a pixel having the mean value for the four pixel values, represented by

$$g_M(x,y) = \frac{1}{4} \sum_{i,j \in R_{22}} g_H(2x - i, 2y - j) \tag{11}$$

where R_{22} is a 2-by-2-pixel region. The medium-resolution image is enlarged by up-sampling with pixel substitution, i.e., a pixel in the medium-resolution image is replaced by four pixels with the same pixel value, as follows:

$$g_M^U(x,y) = g_M\left(\frac{x}{2}, \frac{y}{2}\right). \tag{12}$$

Then, a high-resolution difference image $d_H(x,y)$ is obtained by subtraction of the enlarged medium-resolution image from the high-resolution image, represented by

$$d_H(x,y) = g_H(x,y) - g_M^U(x,y). \tag{13}$$

These procedures are performed repeatedly, producing further lower-resolution images. Thus, multiresolution images having

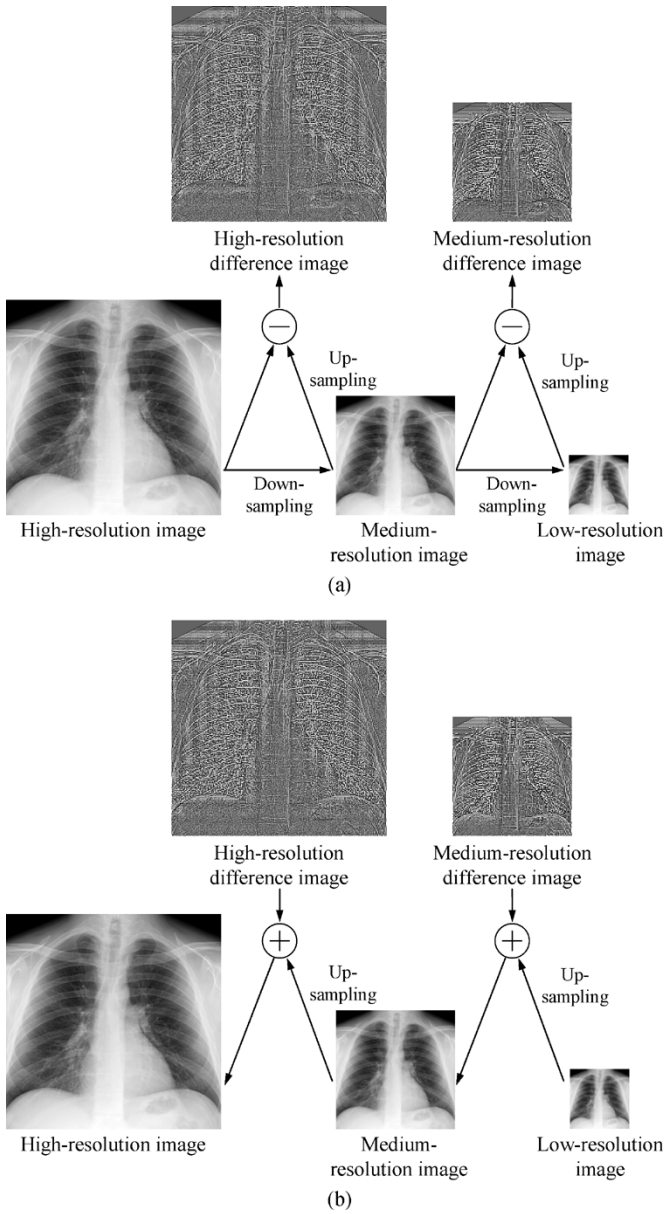

Fig. 2. Illustrations of (a) a multiresolution decomposition technique and (b) a multiresolution composition technique. Lower-resolution images are produced by repeatedly performing down-sampling and subtracting in a multiresolution decomposition technique. Exactly the same original resolution image can be obtained from the multiresolution images by performing a multiresolution composition technique.

various frequencies are obtained by use of the multiresolution decomposition technique.

An important property of this technique is that exactly the same original-resolution image $g_H(x,y)$ can be obtained from the multiresolution images, $d_H(x,y)$ and $g_M(x,y)$, by performing the inverse procedures, called a multiresolution composition technique as shown in Fig. 2(b), as follows:

$$g_H(x,y) = g_M\left(\frac{x}{2},\frac{y}{2}\right) + d_H(x,y). \tag{14}$$

Therefore, we can process multiresolution images independently instead of processing original high-resolution images directly; i.e., with these techniques, the processed original high-resolution image can be obtained by composing of the processed multiresolution images. An MTANN only needs to support a limited spatial frequency rage in each resolution image instead of the entire spatial frequencies in the original image.

C. Multiresolution MTANN for Suppressing Ribs

Fig. 3 illustrates the architecture and training of a multiresolution MTANN involving multiresolution decomposition/composition techniques and MTANNs for different-resolution images. First, input chest radiographs and the corresponding teaching bone images are decomposed into sets of different-resolution images, and then these sets of images are used for training three MTANNs in the multiresolution MTANN, as illustrated in Fig. 3(a). Each MTANN is an expert for a certain resolution, i.e., a low-resolution MTANN is in charge of low-frequency components of ribs, a medium-resolution MTANN is for medium-frequency components, and a high-resolution MTANN for high-frequency components. Each resolution MTANN is trained independently with the corresponding resolution images. After training, the MTANNs produce different-resolution images, and then these images are composed to provide a complete high-resolution image by use of the multiresolution composition technique, as illustrated in Fig. 3(b). The complete high-resolution image is expected to be similar to the teaching bone image; therefore, the multiresolution MTANN would provide a "bone-image-like" image in which ribs are separated from soft tissues.

The multiple MTANN scheme in our previous studies [37]–[40] was developed for classification of candidates into multiple categories; therefore, the output of the multiple MTANN scheme is a class, i.e., abnormal or normal, whereas the output of the multiresolution MTANN is a pixel value. In the multiple-MTANN scheme, MTANNs were combined with scoring, thresholding, and the logical AND operation, whereas the multiresolution MTANN does not use any of these. In the multiresolution MTANN, the input to each of MTANNs is certain frequency components obtained from the original images by use of the multiresolution decomposition, whereas the input of the multiple MTANN scheme is pixel values of the original images.

In this paper, we focused on the suppression of ribs and clavicles in lung regions, because most nodules overlapping with these structures are in the lung regions. For processing only in the lungs, lung regions are segmented by thresholding.

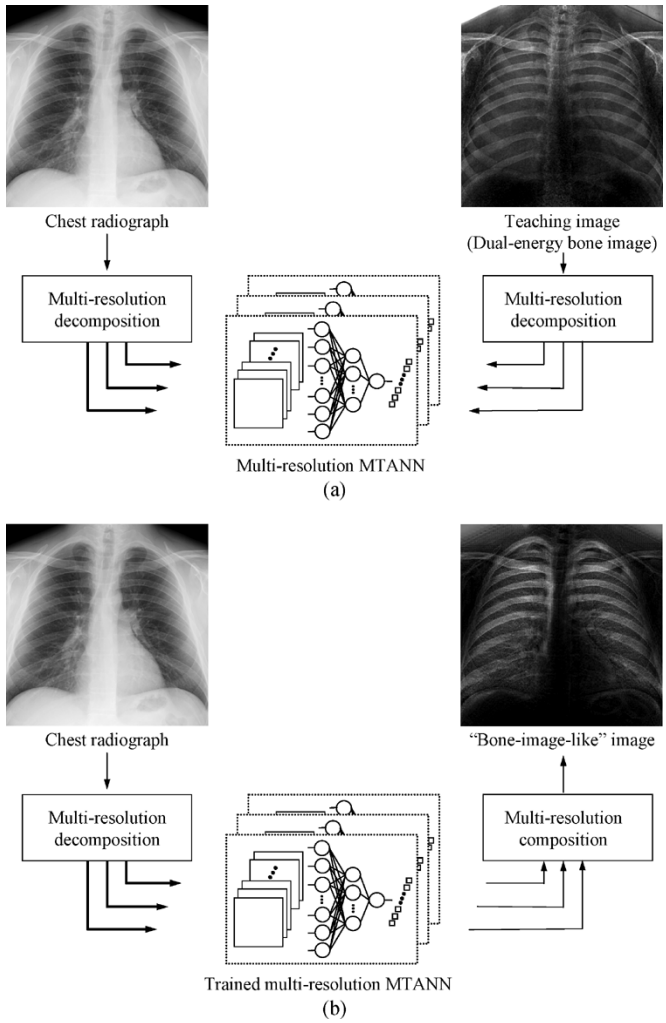

Fig. 3. Diagrams of (a) a training phase and (b) an execution phase of a multiresolution MTANN consisting of MTANNs for different-resolution images. In the training phase, an input chest radiograph and a teaching bone image are decomposed into multiresolution images by use of a multiresolution decomposition technique. Each of the multiresolution images is used for each of the corresponding resolution MTANNs in the multiresolution MTANN. In the execution phase, the output multiresolution images of the trained multiresolution MTANN are composed to provide a "bone-image-like" image by use of a multiresolution composition technique.

A threshold value is determined by use of a method [47] based on linear discriminant analysis (LDA), which is a common method in the fields of computer vision and pattern recognition (often referred as Otsu thresholding). It is expected that a reasonable threshold value can be determined by use of LDA, because threshold determination can be considered as a two-class classification problem in the domain of the histogram of gray levels, and the linear separation with LDA would work well in this one dimensional space. This method automatically selects the lowest point between two classes in the histogram of gray levels in a chest radiograph (i.e., this is formulated as LDA). The method involves minimizing the ratio of between-class variance to the total variance. After the segmentation, a Gaussian filter is applied for smoothing the edges of the segmented lung regions to create an image $m(x,y)$ for masking the outside of the lung regions. The masking image is normalized to have values from 0 to 1. For suppression of

ribs in an original chest radiograph, the bone-image-like image $f_b(x,y)$ produced by the multiresolution MTANN is subtracted from the original chest radiograph $g(x,y)$ with the masking image $m(x,y)$ as follows:

$$f_S(x,y) = g(x,y) - w_C \times f_b(x,y) \times m(x,y) \qquad (15)$$

where w_C is a weighting parameter for determining the contrast of ribs. By changing the weighting parameter w_C, one can obtain processed chest radiographs with different contrast of ribs. Thus, the multiresolution MTANN would be able to produce a "soft-tissue-image-like" image where ribs are suppressed; therefore, this image processing may be considered as a "rib suppression" technique.

D. Database

The database used in our study consisted of 122 posterior-anterior chest radiographs acquired with a computed radiography system with a dual-energy subtraction unit (FCR 9501 ES; Fujifilm Medical Systems, Stamford, CT) at The University of Chicago Hospitals. The dual-energy subtraction unit employed a single-shot dual-energy subtraction technique where image acquisition is performed with a single exposure that is detected by two receptor plates separated by a filter for obtaining images at two different energy levels [44], [48], [49]. The chest radiographs included 121 abnormal cases with pulmonary nodules and a "normal" case (i.e., a nodule-free case). The matrix size of the chest images was 1,760 × 1,760 pixels (pixel size, 0.2 mm; gray scale, 10 bits). The absence and presence of nodules in the chest radiographs were confirmed by use of CT examinations. Most nodules overlapped with ribs and/or clavicles in chest radiographs. In order to train a multiresolution MTANN, we used a training set consisting of four chest radiographs and the corresponding dual-energy soft-tissue and bone images. Three of the four chest radiographs were from nodule cases, and the other was the normal case. The registration error between the input images and the teaching images would be minimum because of the use of the single-shot dual-energy subtraction technique. We used a test set consisting of 118 nodule cases for testing our technique. For computational efficiency, the size of the chest radiographs was reduced by a factor of four, i.e., 440 × 440 pixels.

We used another test set consisting of 136 digitized screen-film chest radiographs with 136 solitary pulmonary nodules, which was the Digital Image Database developed by the Japanese Society of Radiological Technology (JSRT) [50], a publicly available database. The chest radiographs were collected from 14 medical institutions. The absence and presence of nodules in the chest radiographs were confirmed by CT. The locations of all nodules were confirmed by three chest radiologists. The chest radiographs were digitized with a 0.175-mm pixel size, a matrix size of 2,048 × 2,048, and a 12-bit gray-scale level. The sizes of nodules ranged from 8.9 to 29.1 mm, and the average size was 17.4 mm. The database contained 64 malignant and 27 benign nodules, which were confirmed by histologic or cytologic examinations or follow-up imaging. For computational efficiency, the size of the chest radiographs was reduced by a factor of four to 512 × 512 pixels with a 10-bit gray-scale level by use of averaging.

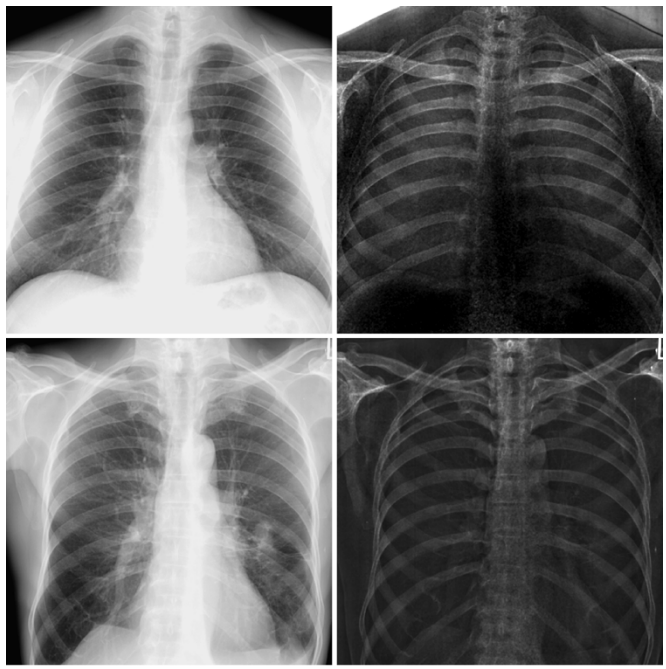

(a) (b)

Fig. 4. Illustrations of (a) input images and (b) the corresponding teaching bone images used for training a multiresolution MTANN (upper images: a normal case; lower images: a nodule case).

III. Results

A. Training

We used four chest radiographs and the corresponding dual-energy bone images in a training set for training a multiresolution MTANN. One of the important properties of an MTANN is that it can be trained with a very small number of cases, because an MTANN is trained with a large number of subregions extracted from input images, i.e., an MTANN can be trained not on a case base, but on a subregion base [51]. We used one typical normal case and three cases with nodules as training cases. Fig. 4 shows the normal case and an example of a nodule case.

For training of the features in lung regions, 5,000 pairs of training samples were extracted randomly from manually traced lung regions in each of the multiresolution images. Training samples for nodules were extracted from the manually traced nodule regions which were large enough to cover the nodules. We combined these training samples and used them for training a multiresolution MTANN. We determined the size R_S of the subregions of MTANNs to be nine by nine pixels, so that the sub-region was sufficient to cover the width of a rib in the low-resolution image. We used three-layered MTANNs where the numbers of input, hidden, and output units were 81, 20, and 1, respectively. The learning rate was 0.001. With the parameters above, training of three MTANNs was performed 1 000 000 times, and the training converged with mean absolute errors of 0.081, 0.086, and 0.017.

Fig. 5(a) shows the composed output image, i.e., a bone-image-like image, of the trained multiresolution MTANN. Ribs are extracted effectively in the bone-image-like image, and this image is similar to the dual-energy bone image shown in Fig. 4(b) (upper image). Ribs in the bone-image-like image

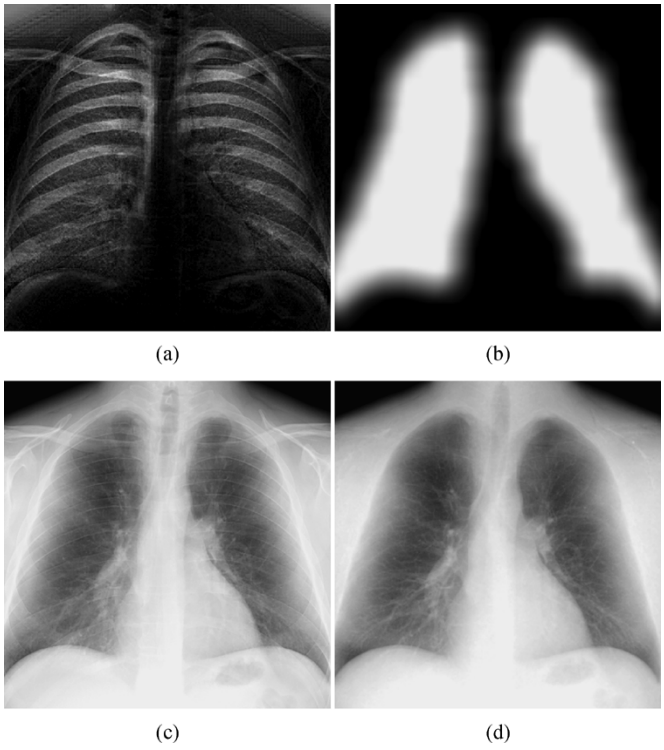

Fig. 5. Illustrations of (a) the output image, i.e., a bone-image-like image, of the trained multiresolution MTANN for the upper image in Fig. 4 (a), (b) a masking image for lung regions, (c) a soft-tissue-image-like image obtained by use of our technique, and (d) the corresponding dual-energy soft-tissue image.

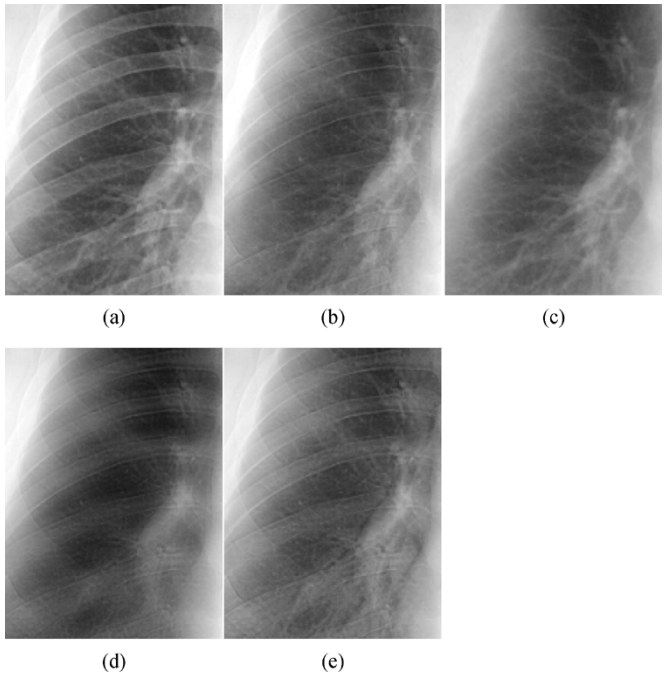

Fig. 6. Comparisons among (a) an original image (region-of-interest; ROI) extracted from the upper image in Fig. 4 (a), (b) a soft-tissue-image-like image obtained by use of our technique, (c) a dual-energy soft-tissue image, (d) the output image of the optimized linear filter, and (e) the output image of a single MTANN without multiresolution decomposition/composition techniques.

are relatively noisy compared to the dual-energy bone image. Delicate parts of small vessels remain in the bone-image-like image, which causes the noisy opacity. It will be noted that bones outside the lung regions, such as parts of clavicles and the spinal column, were not enhanced in the bone-image-like image, because the training was limited to the lung regions. Fig. 5(c) shows a soft-tissue-image-like image obtained by use of a weighting parameter of 1.0 and the masking image shown in Fig. 5(b). The contrast of ribs is substantially suppressed in the soft-tissue-image-like image, whereas the visibility of soft tissues such as lung vessels is maintained. The soft-tissue-image-like image is very similar to the corresponding dual-energy soft-tissue image shown in Fig. 5(d).

We compared the trained multiresolution MTANN with the linear filter optimized under the least-mean-square error criterion [52] with the same training images as used for the MTANN. The linear filter consisted of nine-by-nine inputs I_n with 81 weights w_n, represented by

$$L(x,y) = \sum_{n=1}^{81} I_n \cdot w_n \tag{16}$$

where $\{I_1, I_2, \cdots, I_n, \cdots, I_{81}\} = \{g(x-i, y-j) | i, j \in R_L\}$, and R_L is a nine-by-nine input region. Fig. 6 shows comparisons between the trained multiresolution MTANN and the optimized linear filter. Ribs are suppressed substantially in the output image of the trained multiresolution MTANN, while maintaining the visibility of vessels. The edges of ribs in the output image of the optimized linear filter appear to be doubled and blurred. Moreover, vessels almost disappear. It should be noted that the output images of the optimized linear filter for other chest images had similar visibility of ribs and vessels. This result indicated that the capability of the linear filter was not sufficient for separating ribs in chest radiographs.

Moreover, we investigated the effect of multiresolution decomposition/composition techniques on the performance of an MTANN. We trained a single MTANN with the same training images without the use of multiresolution decomposition/composition techniques. The parameters for the single MTANN were the same as those for the multiresolution MTANN. Fig. 6(e) shows the output image of the trained single MTANN. Parts of ribs are suppressed in the output image, whereas some vessels disappear. This result indicates that the use of multiresolution decomposition/composition techniques in MTANNs improved the performance in the suppression of ribs and the maintenance of soft-tissue opacities.

B. Evaluation

We applied the trained multiresolution MTANN to a validation test set that included 118 nodule cases. The performance was evaluated quantitatively by use of a normalized mean absolute error between bone-image-like images $f_b(x,y)$ and the corresponding dual-energy bone images $b(x,y)$, represented by

$$E_N = \frac{\sum_{x,y \in R_L} |b(x,y) - f_b(x,y)|}{N_L(b_{\max} - b_{\min})} \tag{17}$$

where R_L indicates lung regions, N_L is the number of pixels in R_L, and $b_{\max}$ and $b_{\min}$ are the maximum value and the minimum value in R_L in the dual-energy bone image, respectively. We used bone-image-like images and dual-energy bone images

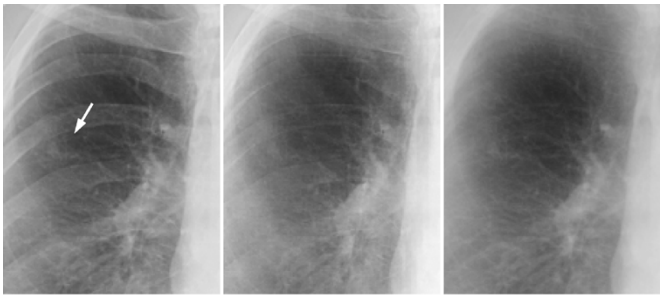

Fig. 7. Result for a nontraining chest radiograph with the best average normalized error ($E_N = 0.061$) among 118 nodule cases in a validation test. Illustrations of (a) an original chest radiograph (nodule is indicated by an arrow), (b) a soft-tissue-image-like image obtained by use of our technique, and (c) the corresponding dual-energy soft-tissue image.

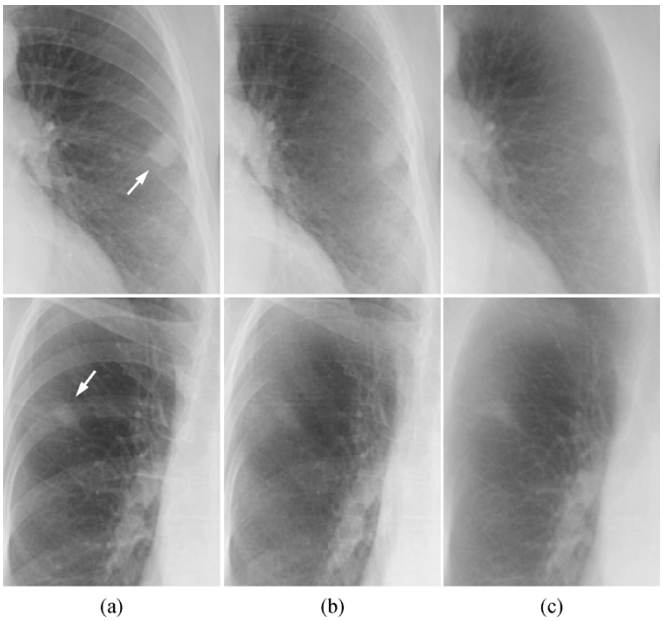

Fig. 8. Results for nontraining chest radiographs with about a middle ranking in average normalized errors ($E_N = 0.078$ and 0.080 for the upper case and the lower case, respectively) among 118 nodule cases in a validation test. Illustrations of (a) original chest radiographs (nodule is indicated by an arrow), (b) soft-tissue-image-like images obtained by use of our technique, and (c) the corresponding dual-energy soft-tissue images.

in this evaluation, because the direct comparison with the output images of the multiresolution MTANN would be more accurate compared to the use of soft-tissue-image-like images, e.g., soft-tissue-image-like images can differ when a weighting parameter is changed. The result for the 118 chest radiographs was an average E_N of 0.082 with a standard deviation of 0.014.

Figs. 7–9 show the soft-tissue-image-like images and the corresponding dual-energy soft-tissue images. Fig. 7 shows a case with the best E_N value among the 118 nodule cases, which is 0.061. The contrast of ribs is substantially suppressed in the soft-tissue-image-like image, while the visibility of soft tissues such as lung vessels is mostly maintained. The soft-tissue-image-like image is very similar to the dual-energy soft-tissue image. Fig. 8 illustrates cases with about a middle ranking in E_N values, which are 0.078 and 0.080. In original chest radiographs shown in Fig. 8(a), a nodule

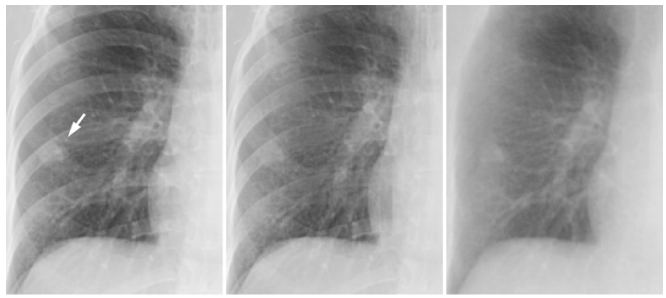

Fig. 9. Result for a nontraining chest radiograph with the worst average normalized error ($E_N = 0.139$) among 118 nodule cases in a validation test. Illustrations of (a) an original chest radiograph (nodule is indicated by an arrow), (b) a soft-tissue-image-like image obtained by use of our technique, and (c) the corresponding dual-energy soft-tissue image.

overlaps completely with an anterior rib and partly with posterior ribs in the upper case, and a nodule overlaps with a posterior rib in the lower case. In the soft-tissue-image-like images, the opacities of the overlapping ribs are compensated for substantially, and the true shapes of the nodules are evident. Thus, the distinction between nodules overlapping with ribs and other anatomic structures is improved in the soft-tissue-image-like images. Fig. 9 shows a case with the worst E_N value, which is 0.139. The ribs are not suppressed very much in the soft-tissue-image-like image in this case. Our technique did not work well for this case, probably because the contrast of ribs in the original chest radiograph of this case was higher than that in other chest radiographs due to the patient's spare frame, i.e., the acquisition condition would be different, and the clavicles at an acute angle indicated that this case would be taken for some special purpose. By inclusion of cases with high rib contrast in training cases, the performance of a multiresolution MTANN for such cases would be improved.

To investigate the robustness of our technique, we performed another experiment with an independent test database including 136 nodule cases obtained from 14 medical institutions [50]. These cases were digitized from films and were acquired at various settings with various systems. We applied the trained multiresolution MTANN to the independent test database. The performance regarding the nodule visibility was evaluated quantitatively by use of a nodule contrast defined by the difference between an average gray level in a nodule region g_N and a background gray level g_B, represented by $C = g_N - g_B$. The nodule region was determined by two expert chest radiologists by the following method: One of the two radiologists determined an initial nodule region, and then the final nodule region was determined by modifying of the initial nodule region by a consensus between the two radiologists. The background gray level was determined as a pixel value at the lower 10% in the histogram of pixel values in a background region in order to avoid the effect of noise. The background region was determined as a belt-like region with a 10 mm width which was obtained by subtracting the nodule region from the dilated nodule region. To evaluate how much the contrast of a nodule is maintained, we defined a nodule contrast ratio represented by $C_R = C_M/C_O$, where C_M is the nodule contrast in an MTANN soft-tissue-image-like image, and C_O is the nodule contrast in an original chest image.

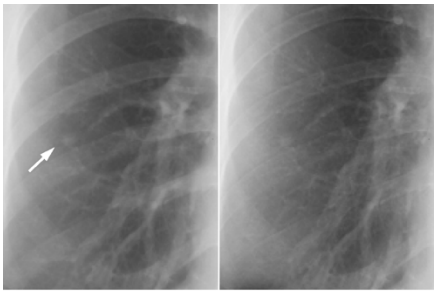

(a) (b)

Fig. 10. Result for a nontraining chest radiograph with the best nodule contrast ratio ($C_R = 1.139$) among 136 nodule cases in an independent test. Illustrations of (a) an original chest radiograph (nodule is indicated by an arrow) and (b) a soft-tissue-image-like image obtained by use of our technique.

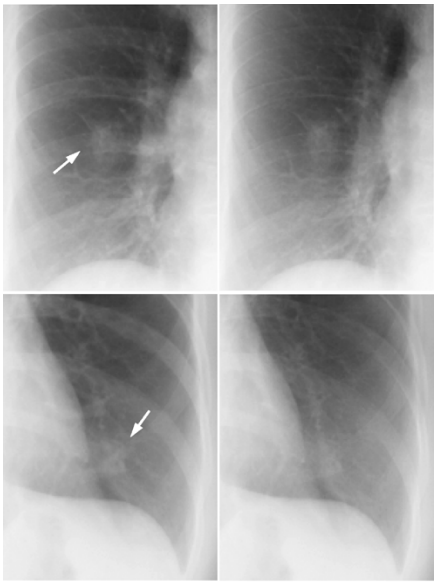

(a) (b)

Fig. 11. Results for nontraining chest radiographs with about a middle ranking in the nodule contrast ratio (both $C_R = 0.897$) among 136 nodule cases in an independent test. Illustrations of (a) original chest radiographs (nodule is indicated by an arrow) and (b) soft-tissue-image-like images obtained by use of our technique.

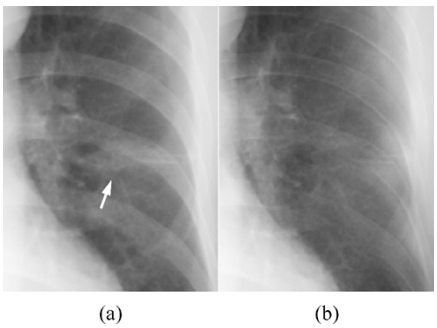

(a) (b)

Fig. 12. Result for a nontraining chest radiograph with the worst nodule contrast ratio ($C_R = 0.620$) among 136 nodule cases in an independent test. Illustrations of (a) an original chest radiograph (nodule is indicated by an arrow) and (b) a soft-tissue-image-like image obtained by use of our technique.

An average nodule contrast ratio over 136 nodules was 0.906 with a standard deviation of 0.155. Figs. 10–12 show soft-tissue-image-like images and the corresponding dual-energy soft-tissue images. Fig. 10 shows a case with the best C_R value among the 136 nodule cases, which is 1.139. The contrast of ribs is suppressed substantially in the soft-tissue-image-like image, whereas the contrast of a nodule is maintained. Thus, the visibility of the nodule is improved by suppression of the ribs around the nodule. Fig. 11 illustrates two cases with about a middle ranking in C_R values, which are both 0.897. The contrast of nodules is mostly maintained in the soft-tissue-image-like images, whereas overlapping ribs are suppressed substantially. Fig. 12 shows a case with the worst C_R value, which is 0.620. The ribs are suppressed in the soft-tissue-image-like image, whereas most parts of the nodule disappear. Our technique did not work well for this case, probably because this particular nodule had characteristics similar to those of ribs in terms of (a) the shape of the nodule, (b) the contrast, (c) the orientation (which is similar to that of a rib in the right lung), (d) the texture (which is smooth), and (e) the margin (which is relatively lighter than its interior).

IV. Discussion

A dual-energy subtraction technique [53], [54] has been used to address the issue of obscuring bones. Dual-energy chest radiographs can be obtained by either a rapid sequence of two exposures, each at a different energy level [e.g., one at 60–80 kV and the other at 110–150 kV] [55]–[58], or a single exposure that is detected by two receptor plates separated by a filter for obtaining images at two different energy levels [44], [48], [49]. Dual-energy soft-tissue images can improve the detection of focal soft-tissue opacities, such as lung nodules, that may be partly obscured by overlying ribs or clavicles [29], [30], [59]. In spite of the advantages, a very limited number of hospitals use radiography systems with dual-energy subtraction, because specialized equipment for obtaining dual-energy X-ray exposures is required. Also, the radiation dose can be greater than that for standard chest radiography in some cases. In addition, the subtraction of two-energy images causes an increased noise level in the images. For improvement in the signal-to-noise ratio, in previous studies, the average skin entrance radiation dose with the two-exposure dual-energy technique was 119 to 130 mR [60], [61], and that with the single-exposure dual-energy technique was 60–100 mR [44], both of which are greater than the 15–20 mR used in standard chest radiography. In a recent study, a 2.4 times higher radiation dose was used for dual-energy radiography compared with conventional radiography in order to obtain the same noise level [62]. The major advantages of our technique compared to a dual-energy subtraction technique are that our technique requires no additional radiation dose to patients, but uses only chest radiographs acquired with a standard radiography system for producing soft-tissue-image-like images; and no specialized equipment for generating dual-energy x-ray exposures, but only software, is required.

A current limitation of conventional chest radiography would be a relatively low sensitivity for detection of early cancer. Likewise dual-energy soft-tissue images, MTANN soft-tissue-image-like images have a potential to improve the sensitivity in detecting early cancer that is partly obscured by overlying ribs, and a potential to improve the specificity by differentiating nodules from other abnormalities or normal

anatomic structures better because of the suppression of obscuring ribs.

We obtained bone-image-like images and soft-tissue-image-like images by use of our technique that was trained with dual-energy bone images. We investigated the effect of the direct use of dual-energy soft-tissue images as the teaching images for a multiresolution MTANN. In the soft-tissue-image-like images obtained by use of the multiresolution MTANN trained with dual-energy soft-tissue images, the contrast of lung vessels was relatively low, and some details of the soft tissue disappeared. The use of dual-energy soft-tissue images as the teaching images was not effective compared to the use of dual-energy bone images, probably because the pattern variations of soft tissues are greater than those of ribs. One advantage of training with dual-energy bone images is that a different contrast of ribs can be obtained by changes in a weighting parameter in the subtraction process used for our technique.

Our technique, likewise the dual-energy subtraction technique, can be sensitive to noise due to subtraction. However, our technique uses standard-dose chest radiographs as input, whereas the dual-energy subtraction technique uses two half-dose chest images and subtracts them. Therefore, our technique would be advantageous, in theory, in terms of the quantum noise level. One way of improving the quantum noise property of both techniques would be to acquire chest images with a higher radiation dose.

We used a very small number of cases for training the multiresolution MTANN, and the multiresolution MTANN produced reliable results for nontraining cases. However, a multiresolution MTANN would be more robust against variations among cases if a larger number of cases were used for training.

A major challenge in current CAD schemes is the detection of nodules overlapping with ribs and clavicles, because most false positives are caused by these structures [18], [28], [39]. Consequently, some researchers have investigated CAD schemes for detection of nodules on dual-energy radiographs [63], [64]. The distinction between nodules and other anatomic structures such as ribs and clavicles is improved in soft-tissue-image-like images with our technique; therefore, these images have the potential to improve the performance of nodule-detection CAD schemes.

Because the use of a multiresolution MTANN requires only software, this technique can be utilized on an existing viewing workstation. The processing time for creating a soft-tissue-image-like image and a bone-image-like image from a chest radiograph is very short, i.e., 1.63 s on a PC-based workstation (CPU: Intel Pentium IV, 3.2 GHz); thus, the software can be applied prior to interpretation in every case without incurring any delay.

Because the fine structures of soft tissues such as small vessels are mostly maintained in soft-tissue-image-like images, the images could potentially be used for quantitative assessment of interstitial lung diseases which are characterized by fine patterns. If our technique is applied to anatomic regions other than the lungs in x-ray images, training with dual-energy images of these anatomic regions would be required for accurate bone suppression.

The multiresolution decomposition/composition techniques with two down/up-sampling steps allowed MTANNs to support a 28.8-by-28.8 mm square region. The height of a posterior rib would range roughly from 10 to 20 mm. We reduced the size of the original chest images by a factor of four before our technique was applied. Because of this reduction, the pixel size was changed from 0.2 to 0.8 mm. In order to process original-resolution chest images with a pixel size of 0.2 mm, we need two more steps of down/up-sampling to support the height of a rib sufficiently. By use of four steps of down/up-sampling, MTANNs can support a 28.8-by-28.8 $(0.2 \times 9 \times 2^4)$ mm square region in the original-resolution chest images. The number of MTANNs needs to be increased to be five. We expect that the MTANNs with original-resolution chest images would produce better images containing the details of soft tissue because of the use of higher-resolution images.

We employed a three-layer structure for the structure of the MTANNs, because it has been proved theoretically that any continuous mapping can be realized approximately by three-layer ANNs [65], [66]. The number of hidden units was determined by use of a method for determining the structure of ANNs [67]. The method is a sensitivity-based pruning method, i.e., the sensitivity to the training error was calculated when a certain unit was removed experimentally, and the unit with the smallest training error was removed. Removing the redundant hidden units and retraining for recovering the potential loss due to the removal were performed repeatedly, resulting in a reduced structure where redundant units were removed. As a result, the number of hidden units was determined to be 20. Thus, the numbers of units in the input, hidden, and output layers were 81, 20, and 1, respectively.

The training of an MTANN seeks to minimize errors between output images and teaching bone images. The quality of the teaching bone images would affect the output image of the trained MTANN, and thus, the final soft-tissue-image-like images. A way to improve the quality of the teaching bone images would be to acquire teaching bone images with a higher radiation dose to reduce quantum noise. The relatively high-dose bone images should be used only for training. Once training is completed, the trained MTANN can be applied to standard dose chest radiographs.

An MTANN is a highly nonlinear complex model. A complex model usually tends to have a poor generalization ability. If a model (e.g., a standard ANN) is trained with only a small number of samples, the generalization ability will be lower, i.e., the model may fit only the training samples; this is known as "over-training" (or "over-fitting") [68]. This issue often occurs when the number of freedoms (parameters) in a model is greater than the number of training samples. A study showed that a standard ANN with 100 parameters required 400–800 training samples to achieve an adequate performance for nontraining cases [69]. The number of training samples was 4–8 times greater than the number of parameters in the ANN. On the other hand, the results with the independent database in this paper showed that MTANNs have a high generalization ability, which is consistent with what we experienced in other applications [37]–[40]. In our previous study, we found that a key to the high generalization ability of MTANNs is the massive training with a large

number of subregions extracted from images [70]. In this study, the number of training samples for each MTANN, which was 7100 (5000 subregions from a normal case and 2100 subregions from nodule cases), was 4.3 times greater than the number of parameters of the MTANN, which was 1,661. This is within the above range (4–8 times) for obtaining an adequate performance for nontraining cases. Thus, the number of training samples might have reached a necessary number for determining the parameters in the MTANNs adequately.

V. Conclusion

We developed an image-processing technique for suppression of ribs in chest radiographs by means of a multiresolution MTANN. With our technique, rib components in chest radiographs are suppressed substantially, while soft-tissues such as lung nodules and lung vessels are maintained. Therefore, our technique would be potentially useful for radiologists as well as for CAD schemes in the detection of lung nodules in chest radiographs.

Acknowledgment

The authors are grateful to F. Li for her clinical advice, to J. Shiraishi and Q. Li for their valuable suggestions, and to E. F. Lanzl for improving the manuscript.

References

[1] C. J. Murray and A. D. Lopez, "Mortality by cause for eight regions of the world: global burden of disease study," *Lancet*, vol. 349, no. 9061, pp. 1269–1276, 1997.

[2] G. E. Goodman, "Lung cancer. 1: prevention of lung cancer," *Thorax*, vol. 57, no. 11, pp. 994–999, 2002.

[3] A. Jemal, R. C. Tiwari, T. Murray, A. Ghafoor, A. Samuels, E. Ward, E. J. Feuer, and M. J. Thun, "Cancer statistics, 2004," *CA. Cancer J. Clin.*, vol. 54, no. 1, pp. 8–29, 2004.

[4] J. K. Frost, W. C. Ball Jr., M. L. Levin, M. S. Tockman, R. R. Baker, D. Carter, J. C. Eggleston, Y. S. Erozan, P. K. Gupta, and N. F. Khouri *et al.*, "Early lung cancer detection: results of the initial (prevalence) radiologic and cytologic screening in the Johns Hopkins study," *Am. Rev. Respir. Dis.*, vol. 130, no. 4, pp. 549–554, 1984.

[5] R. S. Fontana, D. R. Sanderson, W. F. Taylor, L. B. Woolner, W. E. Miller, J. R. Muhm, and M. A. Uhlenhopp, "Early lung cancer detection: results of the initial (prevalence) radiologic and cytologic screening in the Mayo Clinic study," *Am. Rev. Respir. Dis.*, vol. 130, no. 4, pp. 561–565, 1984.

[6] C. I. Henschke, O. S. Miettinen, D. F. Yankelevitz, D. M. Libby, and J. P. Smith, "Radiographic screening for cancer. Proposed paradigm for requisite research," *Clin. Imag.*, vol. 18, no. 1, pp. 16–20, 1994.

[7] R. T. Heelan, B. J. Flehinger, M. R. Melamed, M. B. Zaman, W. B. Perchick, J. F. Caravelli, and N. Martini, "Non-small-cell lung cancer: results of the New York screening program," *Radiology*, vol. 151, no. 2, pp. 289–293, 1984.

[8] T. Sobue, T. Suzuki, M. Matsuda, T. Kuroishi, S. Ikeda, and T. Naruke, "Survival for clinical stage I lung cancer not surgically treated. Comparison between screen-detected and symptom-detected cases. The Japanese Lung Cancer Screening Research Group," *Cancer*, vol. 69, no. 3, pp. 685–692, 1992.

[9] B. J. Flehinger, M. Kimmel, and M. R. Melamed, "The effect of surgical treatment on survival from early lung cancer. Implications for screening," *Chest*, vol. 101, no. 4, pp. 1013–1018, 1992.

[10] J. H. Austin, B. M. Romney, and L. S. Goldsmith, "Missed bronchogenic carcinoma: radiographic findings in 27 patients with a potentially resectable lesion evident in retrospect," *Radiology*, vol. 182, no. 1, pp. 115–122, 1992.

[11] P. K. Shah, J. H. Austin, C. S. White, P. Patel, L. B. Haramati, G. D. Pearson, M. C. Shiau, and Y. M. Berkmen, "Missed nonsmall cell lung cancer: radiographic findings of potentially resectable lesions evident only in retrospect," *Radiology*, vol. 226, no. 1, pp. 235–241, 2003.

[12] M. L. Giger, K. Doi, and H. MacMahon, "Image feature analysis and computer-aided diagnosis in digital radiography. 3. Automated detection of nodules in peripheral lung fields," *Med. Phys.*, vol. 15, no. 2, pp. 158–166, 1988.

[13] B. van Ginneken, B. M. ter Haar Romeny, and M. A. Viergever, "Computer-aided diagnosis in chest radiography: a survey," *IEEE Trans. Med. Imag.*, vol. 20, no. 12, pp. 1228–1241, Dec. 2001.

[14] K. Abe, K. Doi, H. MacMahon, M. L. Giger, H. Jia, X. Chen, A. Kano, and T. Yanagisawa, "Computer-aided diagnosis in chest radiography. Preliminary experience," *Invest. Radiol.*, vol. 28, no. 11, pp. 987–993, 1993.

[15] T. Kobayashi, X. W. Xu, H. MacMahon, C. E. Metz, and K. Doi, "Effect of a computer-aided diagnosis scheme on radiologists' performance in detection of lung nodules on radiographs," *Radiology*, vol. 199, no. 3, pp. 843–848, 1996.

[16] S. Kakeda, J. Moriya, H. Sato, T. Aoki, H. Watanabe, H. Nakata, N. Oda, S. Katsuragawa, K. Yamamoto, and K. Doi, "Improved detection of lung nodules on chest radiographs using a commercial computer-aided diagnosis system," *AJR Am J Roentgenol*, vol. 182, no. 2, pp. 505–10, 2004.

[17] M. L. Giger, K. Doi, H. MacMahon, C. E. Metz, and F. F. Yin, "Pulmonary nodules: computer-aided detection in digital chest images," *Radiographics*, vol. 10, no. 1, pp. 41–51, 1990.

[18] X. W. Xu, K. Doi, T. Kobayashi, H. MacMahon, and M. L. Giger, "Development of an improved CAD scheme for automated detection of lung nodules in digital chest images," *Med. Phys.*, vol. 24, no. 9, pp. 1395–1403, 1997.

[19] W. A. Lampeter and J. C. Wandtke, "Computerized search of chest radiographs for nodules," *Invest. Radiol.*, vol. 21, no. 5, pp. 384–390, 1986.

[20] S. C. Lo, S. L. Lou, J. S. Lin, M. T. Freedman, M. V. Chien, and S. K. Mun, "Artificial convolution neural network techniques and applications to lung nodule detection," *IEEE Trans. Med. Imag.*, vol. 14, no. 4, pp. 711–718, Dec. 1995.

[21] J. S. Lin, S. C. Lo, A. Hasegawa, M. T. Freedman, and S. K. Mun, "Reduction of false positives in lung nodule detection using a two-level neural classification," *IEEE Trans. Med. Imag.*, vol. 15, no. 2, pp. 206–217, Apr. 1996.

[22] C. E. Floyd, Jr., E. F. Patz Jr., J. Y. Lo, N. F. Vittitoe, and L. E. Stambaugh, "Diffuse nodular lung disease on chest radiographs: a pilot study of characterization by fractal dimension," *AJR. Am. J. Roentgenol.*, vol. 167, no. 5, pp. 1185–1187, 1996.

[23] M. G. Penedo, M. J. Carreira, A. Mosquera, and D. Cabello, "Computer-aided diagnosis: a neural-network-based approach to lung nodule detection," *IEEE Trans. Med. Imag.*, vol. 17, no. 6, pp. 872–880, Dec. 1998.

[24] F. Mao, W. Qian, J. Gaviria, and L. P. Clarke, "Fragmentary window filtering for multiscale lung nodule detection: preliminary study," *Acad. Radiol.*, vol. 5, no. 4, pp. 306–11, 1998.

[25] M. Freedman, S. Lo, F. Lure, X. Xu, J. Lin, H. Zhao, T. Osicka, and R. Zhang, "Computer-aided detection of lung cancer on chest radiographs: algorithm performance vs. radiologists' performance by size of cancer," *Proc SPIE (Medical Imaging: Image Processing)*, pp. 150–159, 2001.

[26] G. Coppini, S. Diciotti, M. Falchini, N. Villari, and G. Valli, "Neural networks for computer-aided diagnosis: detection of lung nodules in chest radiograms," *IEEE Trans. Inf. Technol. Biomed.*, vol. 7, no. 4, pp. 344–357, Dec. 2003.

[27] B. Keserci and H. Yoshida, "Computerized detection of pulmonary nodules in chest radiographs based on morphological features and wavelet snake model," *Med. Image Anal.*, vol. 6, no. 4, pp. 431–447, 2002.

[28] T. Matsumoto, H. Yoshimura, K. Doi, M. L. Giger, A. Kano, H. MacMahon, K. Abe, and S. M. Montner, "Image feature analysis of false-positive diagnoses produced by automated detection of lung nodules," *Invest. Radiol.*, vol. 27, no. 8, pp. 587–597, 1992.

[29] D. L. Ergun, C. A. Mistretta, D. E. Brown, R. T. Bystrianyk, W. K. Sze, F. Kelcz, and D. P. Naidich, "Single-exposure dual-energy computed radiography: improved detection and processing," *Radiology*, vol. 174, no. 1, pp. 243–249, 1990.

[30] F. Kelcz, F. E. Zink, W. W. Peppler, D. G. Kruger, D. L. Ergun, and C. A. Mistretta, "Conventional chest radiography vs dual-energy computed radiography in the detection and characterization of pulmonary nodules," *AJR. Am. J. Roentgenol.*, vol. 162, no. 2, pp. 271–278, 1994.

[31] K. Suzuki, I. Horiba, and N. Sugie, "A simple neural network pruning algorithm with application to filter synthesis," *Neural Process. Lett.*, vol. 13, no. 1, pp. 43–53, 2001.

[32] ——, "Efficient approximation of neural filters for removing quantum noise from images," *IEEE Trans. Signal Process.*, vol. 50, no. 7, pp. 1787–1799, Jul. 2002.

[33] ——, "Neural edge detector—a good mimic of conventional one yet robuster against noise-," in *Lecture Notes in Computer Science*. Berlin, Germany: Springer-Verlag, 2001, vol. 2085, pp. 303–310.
[34] ——, "Neural edge enhancer for supervised edge enhancement from noisy images," *IEEE Trans. Pattern Anal. Mach. Intell.*, vol. 25, no. 12, pp. 1582–1596, Dec. 2003.
[35] K. Suzuki, I. Horiba, N. Sugie, and M. Nanki, "Neural filter with selection of input features and its application to image quality improvement of medical image sequences," *IEICE Trans. Inf. Syst.*, vol. E85-D, no. 10, pp. 1710–1718, 2002.
[36] ——, "Extraction of left ventricular contours from left ventriculograms by means of a neural edge detector," *IEEE Trans. Med. Imag.*, vol. 23, no. 3, pp. 330–339, Mar. 2004.
[37] K. Suzuki, S. G. Armato, F. Li, S. Sone, and K. Doi, "Massive training artificial neural network (MTANN) for reduction of false positives in computerized detection of lung nodules in low-dose CT," *Med. Phys.*, vol. 30, no. 7, pp. 1602–1617, 2003.
[38] H. Arimura, S. Katsuragawa, K. Suzuki, F. Li, J. Shiraishi, S. Sone, and K. Doi, "Computerized scheme for automated detection of lung nodules in low-dose computed tomography images for lung cancer screening," *Acad. Radiol.*, vol. 11, no. 6, pp. 617–629, 2004.
[39] K. Suzuki, J. Shiraishi, H. Abe, H. MacMahon, and K. Doi, "False-positive reduction in computer-aided diagnostic scheme for detecting nodules in chest radiographs by means of massive training artificial neural network," *Acad. Radiol.*, vol. 12, no. 2, pp. 191–201, 2005.
[40] K. Suzuki, F. Li, S. Sone, and K. Doi, "Computer-aided diagnostic scheme for distinction between benign and malignant nodules in thoracic low-dose CT by use of massive training artificial neural network," *IEEE Trans. Med. Imag.*, vol. 24, no. 9, pp. 1138–1150, Sep. 2005.
[41] K. Suzuki, I. Horiba, K. Ikegaya, and M. Nanki, "Recognition of coronary arterial stenosis using neural network on DSA system," *Syst. Comput. Japan*, vol. 26, no. 8, pp. 66–74, 1995.
[42] D. E. Rumelhart, G. E. Hinton, and R. J. Williams, "Learning representations by back-propagating errors," *Nature*, vol. 323, pp. 533–536, 1986.
[43] ——, "Learning internal representations by error propagation," *Parallel Distributed Process.*, vol. 1, pp. 318–362, 1986.
[44] T. Ishigaki, S. Sakuma, Y. Horikawa, M. Ikeda, and H. Yamaguchi, "One-shot dual-energy subtraction imaging," *Radiology*, vol. 161, no. 1, pp. 271–273, 1986.
[45] G. M. Stephane, "A theory for multiresolution signal decomposition: the wavelet representation," *IEEE Trans. Pattern Anal. Mach. Intell.*, vol. 11, no. 7, pp. 674–693, Jul. 1989.
[46] A. N. Akansu and R. A. Haddad, *Multiresolution Signal Decomposition*. Boston, MA: Academic, 1992.
[47] N. Otsu, "A Threshold Selection Method from Gray Level Histograms," *IEEE Trans. Syst., Man, Cybern.*, vol. 9, no. 1, pp. 62–66, Jan. 1979.
[48] T. Ishigaki, S. Sakuma, and M. Ikeda, "One-shot dual-energy subtraction chest imaging with computed radiography: clinical evaluation of film images," *Radiology*, vol. 168, no. 1, pp. 67–72, 1988.
[49] B. K. Stewart and H. K. Huang, "Single-exposure dual-energy computed radiography," *Med. Phys.*, vol. 17, no. 5, pp. 866–875, 1990.
[50] J. Shiraishi, S. Katsuragawa, J. Ikezoe, T. Matsumoto, T. Kobayashi, K. Komatsu, M. Matsui, H. Fujita, Y. Kodera, and K. Doi, "Development of a digital image database for chest radiographs with and without a lung nodule: receiver operating characteristic analysis of radiologists' detection of pulmonary nodules," *AJR Am. J. Roentgenol.*, vol. 174, no. 1, pp. 71–74, 2000.
[51] K. Suzuki, I. S. G. Armato, F. Li, S. Sone, and K. Doi, "Effect of a small number of training cases on the performance of massive training artificial neural network (MTANN) for reduction of false positives in computerized detection of lung nodules in low-dose CT," *Proc. SPIE (Medical Imaging)*, pp. 1355–1366, 2003.
[52] V. Madisetti and D. B. Williams, *The Digital Signal Processing Handbook*. Boca Raton, FL: CRC/IEEE Press, 1998.
[53] R. Glocker and W. Frohnmayer, "Uber die rontgenspektroskopische Bestimmung des Gewichtsanteiles eines Elementes in Gememgen und Verbindungen," *Ann. Physik.*, vol. 76, pp. 369–395, 1925.
[54] B. Jacobson and R. S. Mackay, "Radiological contrast enhancing methods," *Adv. Biol. Med. Phys.*, vol. 6, pp. 201–261, 1958.
[55] L. T. Niklason, N. M. Hickey, D. P. Chakraborty, E. A. Sabbagh, M. V. Yester, R. G. Fraser, and G. T. Barnes, "Simulated pulmonary nodules: detection with dual-energy digital versus conventional radiography," *Radiology*, vol. 160, no. 3, pp. 589–593, 1986.
[56] R. G. Fraser, N. M. Hickey, L. T. Niklason, E. A. Sabbagh, R. F. Luna, C. B. Alexander, C. A. Robinson, A. L. Katzenstein, and G. T. Barnes, "Calcification in pulmonary nodules: detection with dual-energy digital radiography," *Radiology*, vol. 160, no. 3, pp. 595–601, 1986.
[57] N. M. Hickey, L. T. Niklason, E. Sabbagh, R. G. Fraser, and G. T. Barnes, "Dual-energy digital radiographic quantification of calcium in simulated pulmonary nodules," *AJR. Am. J. Roentgenol.*, vol. 148, no. 1, pp. 19–24, 1987.
[58] T. Freund, F. Fischbach, U. Teichgraeber, E. L. Haenninen, H. Eichstaedt, R. Felix, and J. Ricke, "Effect of dose on image quality in a detector-based dual-exposure, dual-energy system for chest radiography," *Acta Radiol.*, vol. 46, no. 1, pp. 41–47, 2005.
[59] J. T. Ho and R. A. Kruger, "Comparison of dual-energy and conventional chest radiography for nodule detection," *Invest. Radiol.*, vol. 24, no. 11, pp. 861–868, 1989.
[60] W. R. Brody, D. M. Cassel, F. G. Sommer, L. A. Lehmann, A. Macovski, R. E. Alvarez, N. J. Pelc, S. J. Riederer, and A. L. Hall, "Dual-energy projection radiography: initial clinical experience," *AJR. Am. J. Roentgenol.*, vol. 137, no. 2, pp. 201–205, 1981.
[61] H. Nishitani, Y. Umezu, K. Ogawa, H. Yuzuriha, H. Tanaka, and K. Matsuura, "Dual-energy projection radiography using condenser x-ray generator and digital radiography apparatus," *Radiology*, vol. 161, no. 2, pp. 533–535, 1986.
[62] G. J. Whitman, L. T. Niklason, M. Pandit, L. C. Oliver, E. H. Atkins, O. Kinnard, A. H. Alexander, M. K. Weiss, K. Sunku, E. S. Schulze, and R. E. Greene, "Dual-energy digital subtraction chest radiography: technical considerations," *Curr. Probl. Diagn. Radiol.*, vol. 31, no. 2, pp. 48–62, 2002.
[63] S. Kido, H. Nakamura, W. Ito, K. Shimura, and H. Kato, "Computerized detection of pulmonary nodules by single-exposure dual-energy computed radiography of the chest (part 1)," *Eur. J. Radiol.*, vol. 44, no. 3, pp. 198–204, 2002.
[64] S. Kido, K. Kuriyama, C. Kuroda, H. Nakamura, W. Ito, K. Shimura, and H. Kato, "Detection of simulated pulmonary nodules by single-exposure dual-energy computed radiography of the chest: effect of a computer-aided diagnosis system (Part 2)," *Eur. J. Radiol.*, vol. 44, no. 3, pp. 205–209, 2002.
[65] K. Funahashi, "On the approximate realization of continuous mappings by neural networks," *Neural Netw.*, vol. 2, pp. 183–192, 1989.
[66] A. R. Barron, "Universal approximation bounds for superpositions of a sigmoidal function," *IEEE Trans. Inf. Theory*, vol. 39, no. 3, pp. 930–945, Mar. 1993.
[67] K. Suzuki, "Determining the receptive field of a neural filter," *Journal of Neural Engineering*, vol. 1, no. 4, pp. 228–237, 2004.
[68] C. M. Bishop, *Neural Networks for Pattern Recognition*. New York: Oxford Univ. Press, 1995.
[69] H. P. Chan, B. Sahiner, R. F. Wagner, and N. Petrick, "Classifier design for computer-aided diagnosis: effects of finite sample size on the mean performance of classical and neural network classifiers," *Med. Phys.*, vol. 26, no. 12, pp. 2654–2668, 1999.
[70] K. Suzuki and K. Doi, "How can a massive training artificial neural network (MTANN) be trained with a small number of cases in the distinction between nodules and vessels in thoracic CT?," *Acad. Radiol.*, vol. 12, no. 10, pp. 1333–1341, 2005.